29.2 A Scalable Quantum Magnetometer in 65nm CMOS with Vector-Field Detection Capability

Mohamed I. Ibrahim, Christopher Foy, Dirk R. Englund, Ruonan Han

Massachusetts Institute of Technology, Cambridge, MA

Room-temperature control and detection of the nitrogen vacancy (NV) center in diamond's spin-state has enabled magnetic sensing with high sensitivity and spatial resolution [1], [2]. However, current NV sensing apparatuses use bulky off-the-shelf components, which greatly increase the system's scale. In [3], a compact platform, which attaches nanodiamond particles to a CMOS sensor, shrinks this spin-based magnetometer to chip scale; however, the optically detected magnetic resonance (ODMR) curve it generates carries large fluctuation leading to inferior sensitivity. In this paper, we present a CMOS-NV quantum sensor with (i) a highly-scalable microwave-delivering structure and (ii) a Talbot-effect-based photonic filter with enhanced green-to-red suppression ratio. The former enables coherent driving of an increased number of NV centers, and the latter reduces the shot noise of the photo-detector caused by the input green laser. In addition, the usage of a bulk diamond also enables vector magnetometry, which allows for the tracking of magnetic objects and navigation. The prototype sensor provides a measured vector-field sensitivity of 245nT/Hz$^{1/2}$.

The NV center in diamond is an optically active point defect (Fig. 29.2.1), which consists of a nitrogen atom and a vacancy that replace an adjacent pair of carbon atoms in the diamond lattice. Figure 29.2.1 also illustrates the NV energy level diagram. It forms a spin triplet at its ground state, with a $|m_s = 0\rangle$ state at its lowest energy and degenerate $|m_s = \pm1\rangle$ states raised by 2.87GHz. An external magnetic field with a component, B_z, along the N-V axis splits the $|+1\rangle$ and $|-1\rangle$ states by $2\gamma_e B_z$, (γ_e= 28GHz/T). Consequently, the NV spin resonance frequencies (f_- and f_+) required to drive these two spin states split from 2.87GHz. The difference between f_- and f_+ is proportional to B_z and can be measured from optical detection of the magnetic resonances (ODMR). This optical detection is accomplished by exciting the NV centers with green excitation, resulting in red fluorescence minima at f_- and f_+. In a bulk diamond, each of the four crystal lattice axes (Fig. 29.2.1) possesses a population of NV centers. To fully reconstruct an applied magnetic-field's direction and magnitude, its projections along each of the NV's axes are measured.

Shown in Fig. 29.2.2, the CMOS quantum sensor is composed of two sub-systems: (i) generation, switching and uniform delivery of ~ 2.87GHz microwave to coherently excite the spin states of the NV ensemble, and (ii) filtering of green excitation and detection of red NV fluorescence. The 2.87GHz microwave signal is generated by an on-chip phase-locked loop (PLL). In [3], a loop inductor was used to deliver the microwave to diamond, but the magnetic field uniformity was sufficient only in a small area within the loop, leading to a lower number, N, of coherently driven NV centers (hence degraded sensitivity: $S_m \propto \sqrt{N^{-1}}$). In this work, an array of current-driven wires is used to synthesize a highly-uniform field in the lateral direction (B_y in Fig. 29.2.3) of the chip's surface. This design stems from the fact that an infinite and uniform current (I_0) array produces a homogeneous transverse magnetic field (Fig. 29.2.3). However, with a finite number of current-driven wires, the field in the vertical direction B_z is no longer fully cancelled and increases towards the array edges. To recover field homogeneity, a few additional wires carrying current larger than I_0 are placed on the edges of the array, providing a ramp-up profile of B_z that cancels the aforementioned vertical field across a wide range of wire array. Our design consists of 32 uniform-current-driven wires (I_0=0.5mA) and 8 field-compensating wires (I_B=3I_0) at each array edge. As shown in the EM simulations and Ampere's law calculations in Fig. 29.2.3, this simultaneously improves the uniformity of B_y and reduces B_z close to zero. The wire currents are regulated by a bank of current sources gated by the PLL output signal. To prevent phase variation of the microwave currents along the Y-axis, the VCO of the PLL is based on a bank of coupled ring oscillators, which are uniformly placed along the Y-axis. The phase noise is subsequently decreased, too.

The incident green light has a much stronger intensity compared to the red fluorescence and adds noise at the sensor output. Previously, a single metal-grating-layer filter based on wavelength-dependent plasmonic loss was used, but its green-to-red rejection ratio (R_{gr}≈10dB) is insufficient [3]. In this work, a multi-grating-layer filter using the Talbot effect is adopted. An incident light upon a grating generates a diffraction pattern, where the intensity maxima and minima repeat in the vertical direction with a wavelength-dependent Talbot length (Fig. 29.2.4). Previously, on-chip Talbot filters were used for angle-sensitive imaging [4]. Here, we strategically place other grating layers in M6 and M3 in positions aligned with the maxima for green wavelength and minima for red wavelength. As the FDTD simulation shows, such a configuration further rejects the green light, in addition to the plasmonic filtering via thick M8 grating layer. The simulated transmission through the filter is 45% for red and 0.05% for green (R_{gr}≈30dB). The pitch in all grating layers is 800nm. Note that the aforementioned current-driven wires plus interleaved dummy wires in M8 form the first photonic filter layer. The spin-dependent red fluorescence is then detected by an on-chip N-well/P-sub photodiode below the optical filter. The photodiode size is 80µm × 300µm. The measured responsivity of the photodiode is 188mA/W.

The quantum sensor is prototyped using a 65nm CMOS technology. The chip has a die area of 1.5mm^2 and consumes 40mA of power in the experiments. A bulk diamond is placed on the chip surface. We introduce a cut in the diamond's corner to direct the incident vertical green laser horizontally. This enhances the overall green rejection. The setup to obtain the ODMR plots is shown in Fig. 29.2.5. A green laser (λ=532nm) is collimated and coupled into the diamond to excite embedded NV centers. Figure 29.2.5 also shows a photo of the setup with green filter on the camera to show the diamond's red fluorescence. The fluorescence collected by the integrated photodiode is measured by a lock-in amplifier. To filter the experimental noise, a frequency-modulated spectroscopy approach is adopted, in which the instantaneous microwave frequency of the chip is modulated with a modulation depth of 6MHz and repetition rate of 3kHz. In addition, differential measurement is done to cancel the green laser variations. A signal source provides both the FM-modulated clock of the PLL and the 3kHz reference to the lock-in amplifier. The lineshape of the measured ODMR is then close to the first-order derivative of the resonances shown in Fig. 29.2.1. First, without applying an external magnetic field, a strong spin resonance is detected at PLL output frequency of 2.87GHz (Fig. 29.2.5). Then, the noise floor of the sensor (σ) is measured (Fig. 29.2.5). Beyond the corner frequency of 3kHz, the sensor white noise is about 0.1µV/Hz^{½}. A magnet placed near the sensor produces four pairs of ODMR dips, corresponding to the four diamond crystal orientations with respect to the magnetic field. The output signal is reduced due to the breaking of the degeneracy of the resonances. This allows the driving of each NV spin population separately. Lastly, the vector-field sensitivity, calculated using the slope of the ODMR curve, m, the measured noise floor, and the constant γ_e, is estimated at 245nT/Hz$^{1/2}$. Figure 29.2.6 summarizes the chip performance in comparison with the prior work [3]. The present device improves sensitivity by 3 orders of magnitude compared to previous CMOS-diamond quantum sensors, while also providing vector-field detection. The current-driven microwave array and photonic filter designs are readily scalable to larger areas for further improvements in sensitivity, or to larger numbers of detectors for gradient magnetometry, multiplexed analytical NMR spectroscopy [5], and other applications [6].

Acknowledgements:
This work is supported by the National Science Foundation (Grant No. 1839159), MIT Center for Integrated Circuits & Systems, Singaporean-MIT Research Alliance, and Master Dynamic Limited. D. E. acknowledges the support of the Army Research Office MURI on "Imaging and Control of Biological Transduction using NV-Diamond". The authors acknowledge Xiang Yi, Donggyu Kim, David Bono, and Cheng Peng at MIT for their technical assistance during prototyping and testing.

References:
[1] J. Taylor, et al., "High-sensitivity diamond magnetometer with nanoscale resolution," *Nature Physics*, vol. 4, no. 10, p. 810, 2008.
[2] G. Balasubramanian, et al., "Nanoscale imaging magnetometry with diamond spins under ambient conditions," *Nature*, vol. 455, no. 7213, p. 648, 2008.
[3] M. I. Ibrahim, et al., "Room-temperature quantum sensing in CMOS: On-chip detection of electronic spin states in diamond color centers for magnetometry," *IEEE VLSI Circuits Symposium,* pp. 249-250, June 2018.
[4] A. Wang, et al., "A light-field image sensor in 180nm CMOS," *IEEE Journal of Solid-State Circuits*, vol. 47, no. 1, pp. 257-271, Jan. 2012.
[5] D. R. Glenn, et al., "High-resolution magnetic resonance spectroscopy using a solid-state spin sensor," *Nature*, vol. 555, no. 7696, p. 351, 2018.
[6] C. L. Degen, et al., "Quantum sensing," *Reviews of modern physics*, vol. 89, no. 3, p. 035002, 2017.

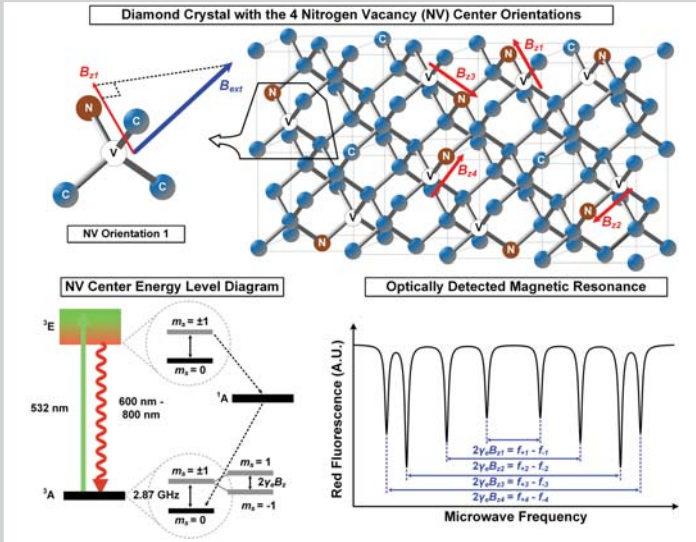

Figure 29.2.1: NV centers in diamond: atomic structure, energy-level diagram and ODMR spectrum with an external field.

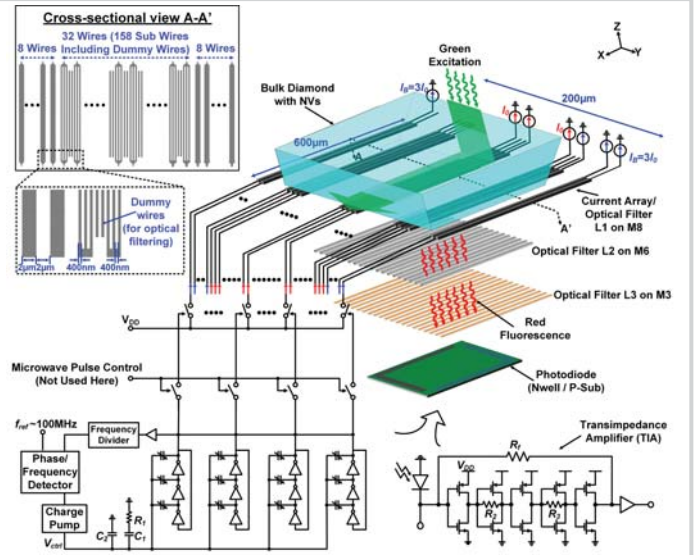

Figure 29.2.2: Schematic of the NV-based magnetic sensor in 65nm CMOS.

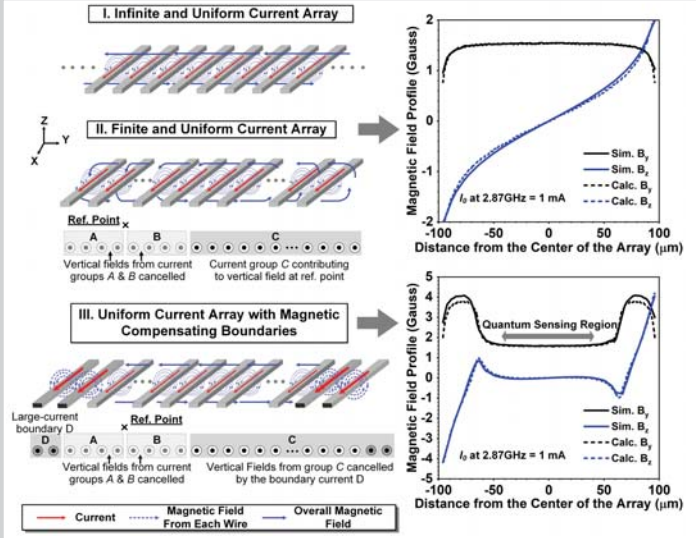

Figure 29.2.3: On-chip current-driven array for high-uniformity magnetic field generation and its field profiles based on EM simulation and calculation.

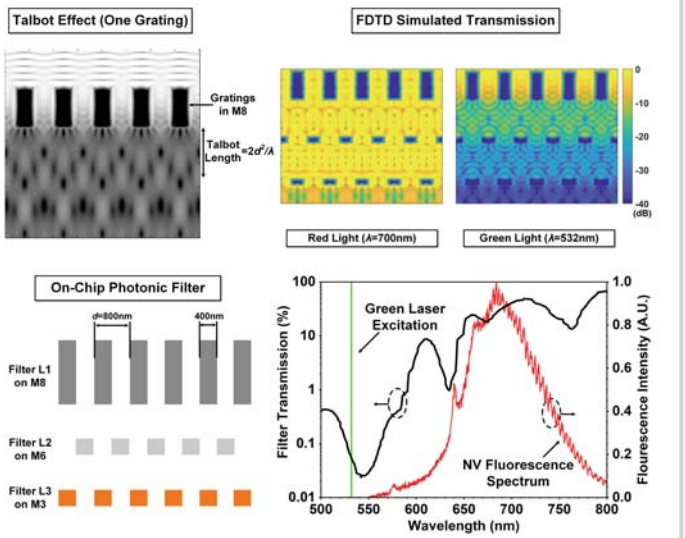

Figure 29.2.4: Design and simulated performance of the multi-layer integrated optical filter based on Talbot effect.

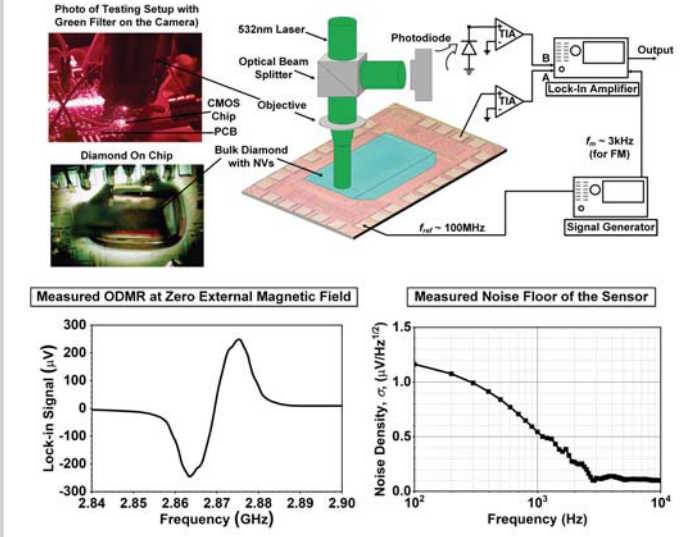

Figure 29.2.5: Test setup of the NV-CMOS magnetometer using frequency modulation, the measured ODMR spectrum and the measured noise floor.

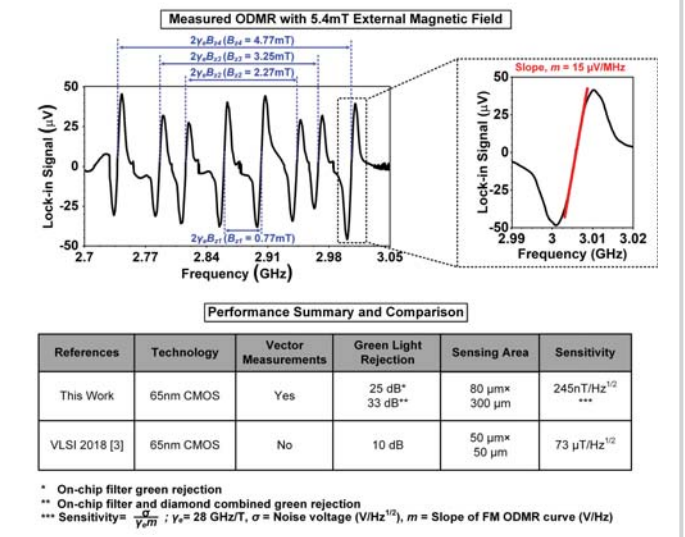

Performance Summary and Comparison

References	Technology	Vector Measurements	Green Light Rejection	Sensing Area	Sensitivity
This Work	65nm CMOS	Yes	25 dB* 33 dB**	80 μm× 300 μm	245nT/Hz$^{1/2}$ ***
VLSI 2018 [3]	65nm CMOS	No	10 dB	50 μm× 50 μm	73 μT/Hz$^{1/2}$

* On-chip filter green rejection
** On-chip filter and diamond combined green rejection
*** Sensitivity= $\frac{\sigma}{\gamma_e m}$; γ_e= 28 GHz/T, σ = Noise voltage (V/Hz$^{1/2}$), m = Slope of FM ODMR curve (V/Hz)

Figure 29.2.6: Measured ODMR spectrum with external magnetic field and a performance summary/comparison table.

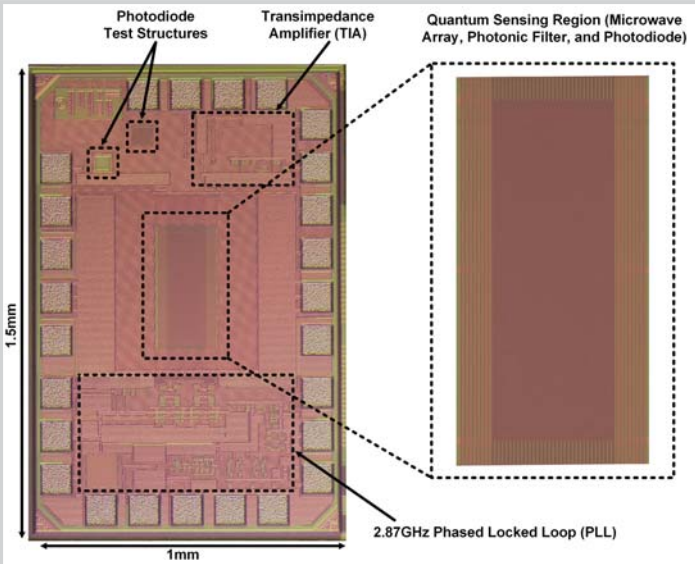

Figure 29.2.7: Die micrograph.

978-1-5386-8531-0/19/$31.00